Aeroacoustics Conferences
June 4-7, 2024, Rome, Italy
30th AIAA/CEAS Aeroacoustics Conference (2024)

10.2514/6.2024-3425

CFD analysis of buzz saw noise employing time-domain non-linear impedance boundary conditions

S.R. Janssen[1], M. Laban[2], and J.C. Kok[3]
Royal Netherlands Aerospace Centre NLR, 1059 CM Amsterdam, the Netherlands

Buzz saw noise emerges in turbofan engines featuring supersonic blade tip speeds and perturbed blade loadings. Such conditions occur at high-power climbing operations and result in considerable noise emissions. This paper employs Computational Fluid Dynamics (CFD) simulation to illustrate the non-linear interaction between the buzz saw noise generating mechanism and acoustic liners in a generic UHBR engine. Blade loading perturbations are modeled by applying blade twist deviations. Additionally, a newly developed time-domain non-linear impedance model is introduced as a boundary condition to incorporate the effects of acoustic liners. The study investigates the impact of both applied twist deviations and liners on the resulting buzz saw noise spectrum. The results demonstrate the capability of CFD simulation to accurately model buzz saw noise. Future research should focus on validating these results, improving the dynamics of the liner model, exploring the benefits of non-uniform liner design, and investigating aeroelastic interactions with liners.

I. Introduction

The issue with aviation noise emissions has spurred significant interest in understanding and mitigating noise sources within aircraft engines. Buzz saw noise, generated by turbofan engines during high-power climbing operations, presents a particular challenge due to its significant contribution to overall noise levels. State-of-the-art simulation models enable airframe integrators to simulate noise generating mechanisms in great detail, providing great benefit early on in the design process.

Buzz saw noise emerges at high power operating conditions during climb or take-off when fan blade tips reach supersonic speeds. The blade tips then feature shocks propagating upstream into the inlet. In an idealized symmetrical fan configuration, the pressure signal at the inlet of the fan-stage consists of a regular sawtooth waveform. The waveform's discontinuities coincide with the shock waves passing by with the blade frequency.

In reality each fan blade features some deviation in blade loading that is the result of manufacturing imperfections. Some blades may display a slightly enhanced loading and increased pressure difference and vice versa. This has two effects that generate buzz saw noise. First, the waveform near the fan is no longer perfectly regular, as each blade features a different pressure jump. Second, the associated shocks propagate upstream at different speeds, altering the interval to neighboring shocks. The latter is the main mechanism that modifies the regular sawtooth near the fan to a highly irregular sawtooth that characterizes buzz saw noise. The mechanism effectively redistributes the acoustic energy of the blade passing frequency to engine order frequencies.

Buzz saw noise generation and propagation was studied in great detail by McAlpine, Fisher, et al. [1]. They stressed the need for '*a more realistic model of the inlet duct … to better predict the attenuation in a lined duct*' as prior approaches were only suitable for symmetric configurations at level flight conditions. This paper introduces a newly developed liner model that responds to local flow conditions (sound pressure level, grazing flow, and wall temperature), making it suitable for non-level non-axisymmetric flight conditions.

[1] R&D Engineer, NLR, Department of Flight Physics and Loads, Stevie.Ray.Janssen@nlr.nl
[2] Senior Scientist, NLR, Department of Flight Physics and Loads, Martin.Laban@nlr.nl
[3] Senior Scientist, NLR, Department of Flight Physics and Loads, Johan.Kok@nlr.nl

The UHBR turbofan engine is one of the modern propulsion concepts that has recently been studied in great detail. Laban et al. [2] use CFD to simulate a generic UHBR model at take-off, approach, and buzz saw flight conditions assessing fan-OGV interaction noise and the impact of bypass duct bifurcations. The aerodynamic performance of an UHBR turbofan model is quantified by Méheut, Laban, Schnell, Lefevre, et al. [3] using various CFD solvers at both design and off-design flight conditions. Daroukh et al. [4] utilize CFD to study the effects of distorted intake flow on shockwaves and tonal noise.

This paper contributes to these advances as it is a first demonstration of simulating buzz saw noise generation and propagation using CFD that includes the non-linear interaction with liner wall treatment. The methods used to simulate buzz saw noise are described, along with an analysis of the role of applied perturbed blade loading and shock propagation on the noise generation mechanism. Additionally, the paper investigates the propagation of buzz saw noise in the near field and provides a brief illustration of the dynamics of the liner. The paper follows the conventional structure of presenting the methodology, results, and discussion.

II. Method

A. UHBR Geometry and Boundary Conditions

The considered configuration is the ASPIRE research engine that was developed by consortium partners in the Clean Sky 2 ASPIRE project. Its interior, core lines, fan exhaust channel, fan- and OGV blades, were designed by DLR. The nacelle and inlet geometry was designed by Airbus. Airbus also delivered the engine operational specifications. The fan stage consists of 16 rotating blades with blade radius about 1.1 m. The OGV stage consists of 36 stator blades, **Fig 1**.

The interior core flow is modelled using outflow and inflow boundary conditions. The core inlet is modelled as a fixed-pressure outflow plane, with pressure level trimmed to match the desired core mass flow. The core outlet is modelled by prescribing total pressure and temperature at the inflow plane. The far field is modelled as a cylindrically shaped artificial boundary with radius roughly 15 times the fan diameter, and height roughly 27.5 times the fan diameter, **Fig 2**. The origin of the fan inlet plane is located at the center of the cylinder. Far field inflow and outflow conditions are prescribed at the artificial boundary. The fan blades and spinner rotate at prescribed rotational velocity. Liner boundary conditions are applied at the intake and fan exhaust duct. The liner model is presented in the appendix, **Eq (1)**. The liner model prescribes a non-zero wall-normal mass flux at the wall. A no-slip condition is enforced simultaneously.

The simulation condition corresponds to high-power operation during take-off or climb, when the fan blade tips exceed the speed of sound. Flight speed equals Mach=0.27 at an altitude of 700ft. The angle-of-attack is 15°, taking into account the effect of wing upwash on the flow at the inlet.

B. Twist Deviation and Blade Stacking

The buzz saw noise generating mechanism does not exist without asymmetries in blade loading. The asymmetry is introduced in the simulation by prescribing a different minor twist deviation angle to each fan blade. A slightly enhanced twist angle induces an increased pressure difference and vice versa. The twist deviation is applied linearly in the blade's spanwise direction, with zero deviation at the root and the prescribed deviation at the tip.

A set of blades with different twist deviation angles can be arranged in azimuth in some stacking order. Changing the stacking order alters the sequence of pressure differences and, consequently, the interval between neighbouring shocks. Hence each stacking corresponds to a different buzz saw noise spectrum. Airbus provided two stacking orders that were used in this work, the so called 'double-angle cosine' and the 'alternate' stackings, **Fig 3**. The 'double-angle cosine' stacking is ordered such that blade-to-blade deviation changes smoothly, reaching extreme values twice in a period. The 'alternate' stacking is ordered such that blade-to-blade deviation is maximized. Both stacking orders are made up of the same set of blade deviation angles.

C. CFD Grid

The multi-block structured CFD grid of the ASPIRE model was constructed by Laban et al. [2], **Fig 4**. The computations were considered at the medium grid level. The intake domain, from highlight plane up to the fan inlet plane, was refined with a factor 2 to enhance the spatial resolution for shocks and acoustic waves, **Fig 5**. The refined fan intake resolution equals 64 cells in axial direction, 112 cells in radial direction, and 1024 cells in azimuth direction. This resolution corresponds to ~64 cells, ~32 cells, and ~24 cells per wavelength of the first three blade passing frequency tones in still air. The complete grid consists of 36.2M cells.

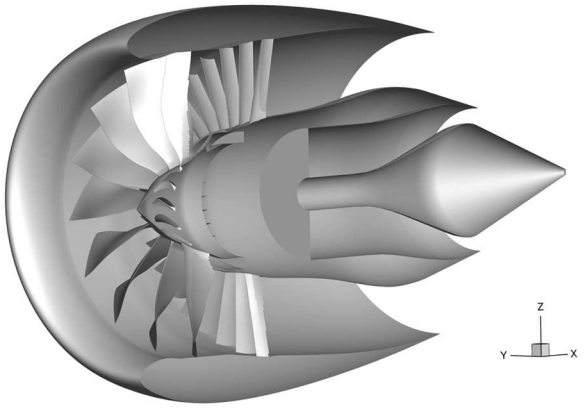

Fig 1 - View of the ASPIRE UHBR geometry

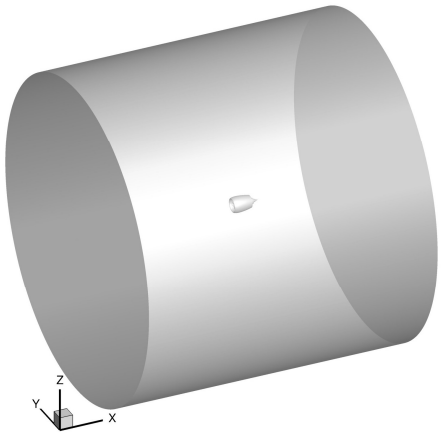

Fig 2 – View of the artificial far-field boundaries

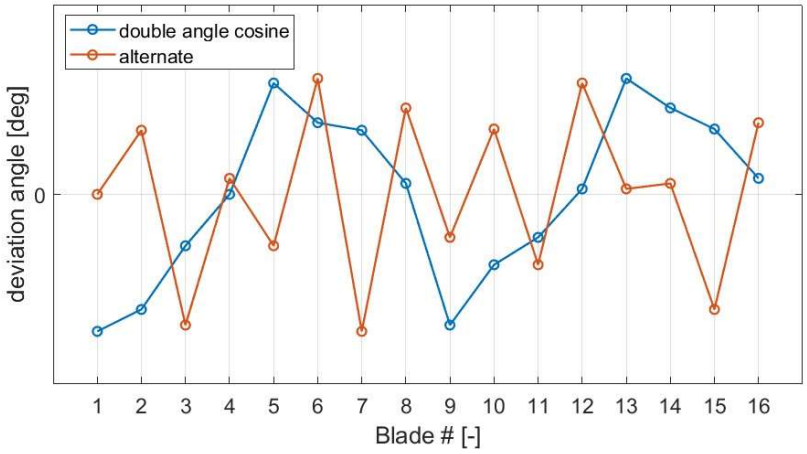

Fig 3 – Stacking orders of the applied blade twist deviation angles. Twist deviations are defined relative to the neutral blade, #1 of the 'double angle cosine' stacking or #4 of the 'alternate' stacking.

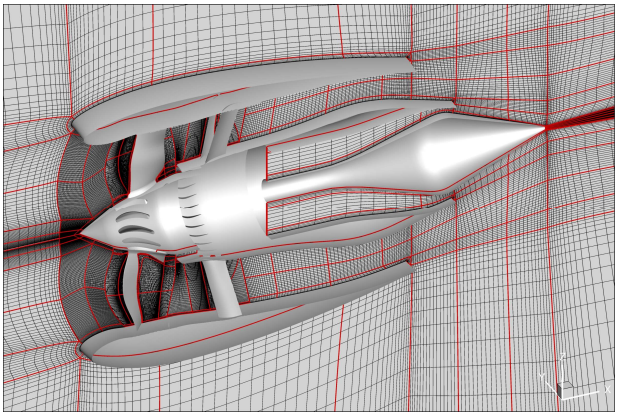

Fig 4 – View of the grid at the engine symmetry plane

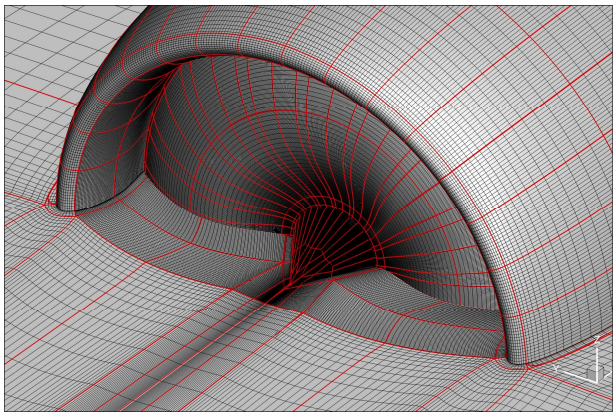

Fig 5 – Close-up of the refined inlet grid up to the fan inlet interface

D. CFD Flow Solver Setup and Solution Procedure

The simulation is computed using NLR's in-house finite-volume CFD solver ENSOLV. The time-dependent RANS equations are solved together with Menter's SST $k-\omega$ turbulence model [5]. A 4th order discretization scheme is used for the convective term. The scheme was designed to minimize numerical dispersion and dissipation, in order to accurately capture the propagation of both acoustic and hydrodynamic modes [6]. The scheme is essentially equivalent to the DRP scheme of Tam and Webb [7] on uniform grids. The diffusive terms and turbulence-model equations are discretized using a standard second-order finite-volume method. Time integration is performed using the second-order implicit scheme with dual time stepping. At each soft-wall boundary face the liner model is solved using the same iterative procedure. The step size is determined using the local eigenvalues of the discretized liner system.

Traditionally a 2-step simulation procedure would be used for the aero acoustic analysis of turbofan configurations. First, a CFD simulation with the unsteady RANS model would be used to simulate the sound generating mechanisms. Second, an acoustic simulation with the linearized Euler equations (LEE) model would be used to simulate the propagation of sound in the near field. This approach relies on the generally valid assumption that the acoustic fluctuations are small enough to allow linearization. In this case, however, it was expected that there is an interaction between the propagating shocks and the liner impedance in the inlet region. The acoustic near field is, therefore, simulated in a single URANS computation. The flow solution was generated by simulating 20 revolutions on the coarser grid level using 360 time steps per revolution, and 20 revolutions on the finer grid level using 720 time steps per revolution. Flow statistics were captured in the final revolution. In total 4 simulations were conducted; the 'double-angle cosine' and 'alternate' blade stacking, with and without liner model active.

III. Results

A. Blade Thrust

The thrust per blade is obtained by integrating the pressure and shear stress contributions at each time step. The obtained periodic thrust signals are presented in **Fig 6a** and **c**. The engine's rotational frequency, i.e. the Engine Order (EO), is the most prominent feature of the periodic signal. The phase of the thrust signal depends on the blade's instantaneous azimuthal position. Maximum thrust is attained when the blade is moving downward, opposing the intake airflow. The mean values display some similarity with the applied stackings, introduced in **Fig 3**. The mean of the 'double-angle cosine' changes smoothly, reaching extreme values twice when going around the blades, whereas the mean of the 'alternate' stacking jumps from blade to blade.

The difference between the liner and hard wall thrust is shown for each blade in **Fig 6b** and **d**. The differences feature dominant modes above the engine order frequency. The mean differences also share similar traits with the applied blade stackings. The phase, however, is different. On average, the liner induced thrust differences seem to oppose the thrust induced by the applied twist deviation. The computed liner induced mean thrust increment equals 0.12% and 0.11% for the 'double-angle cosine' and 'alternate' blade stackings respectively.

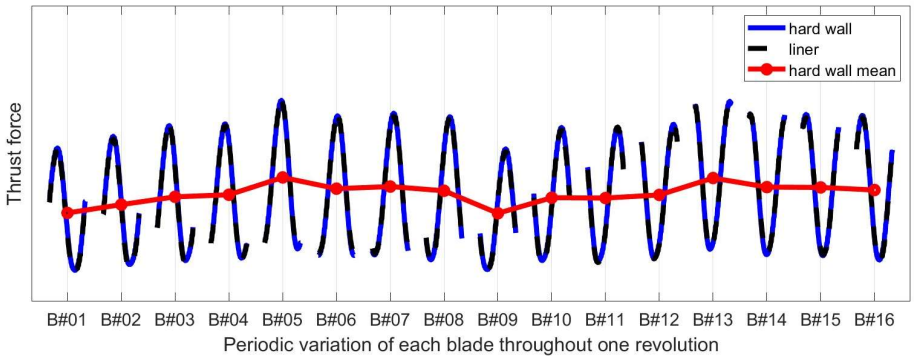

a) thrust force, 'double-angle cosine' stacking

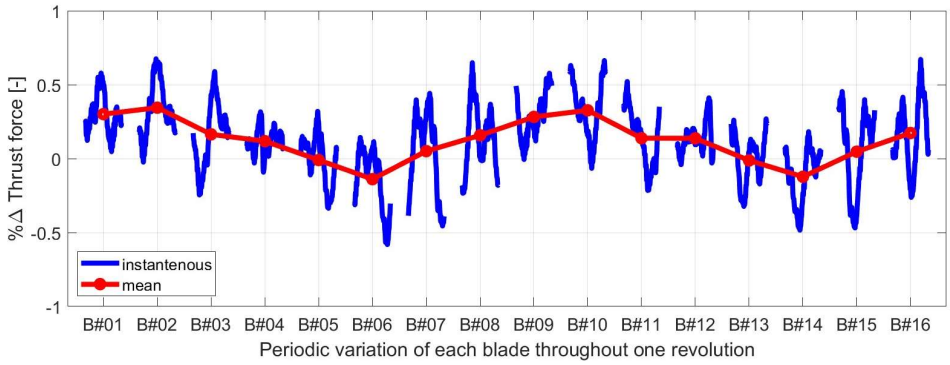

b) thrust difference between liner and hard wall, 'double-angle cosine' stacking

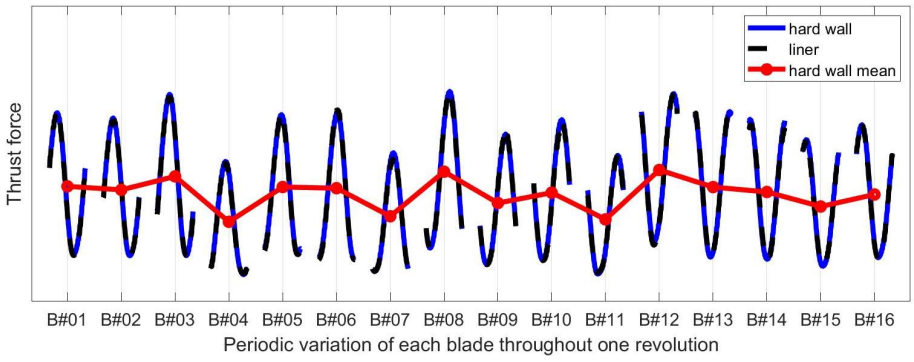

c) thrust force, 'alternate' stacking

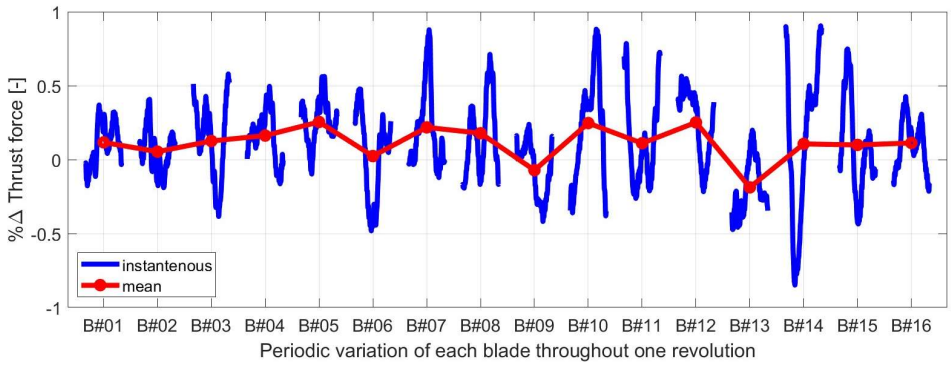

d) thrust difference between liner and hard wall, 'alternate' stacking

Fig 6 – Periodic variations of thrust force for all 16 fan blades (#1-#16 left-to-right). The quantity %Δ*T* is defined as the difference of the liner and hard wall thrust as percentage of the blade's hard wall mean thrust.

B. Investigation of the Shock Pattern

Shocks propagate upstream (negative x-direction) from the blades and bend in the direction opposing the blade rotation, **Fig 7a**. Shockwave strength and directivity varies locally, depending both on azimuth and the applied blade twist deviation. At the crown, the $+90°$ region, the upstream shockwaves propagate towards the highlight. At the keel, the $-90°$ region, shockwaves are blocked by the upstream supersonic inflow over the lower lip's throat section. The shocks in the keel bend in the direction opposing the blade motion, clashing with one another to form a repeating λ−pattern. The liner visibly attenuates shocks upstream, **Fig 7b**.

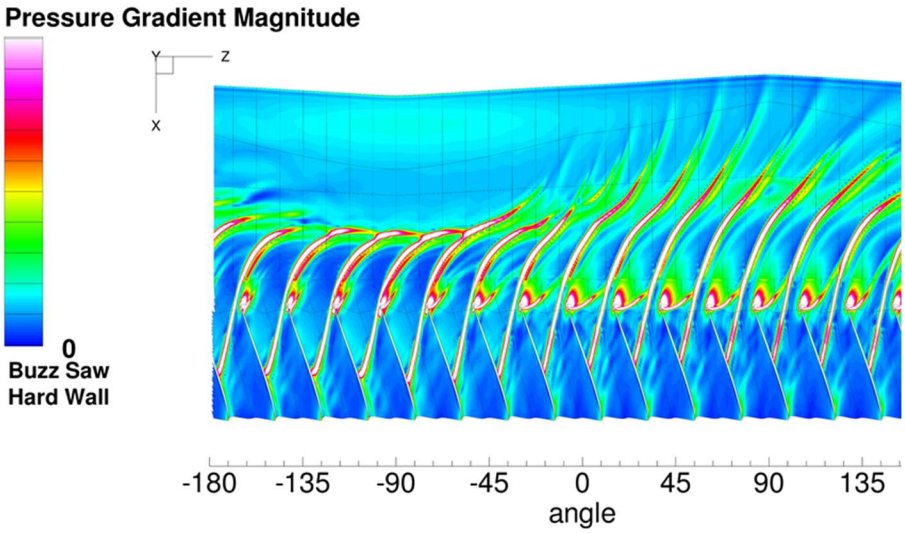

a) hard wall

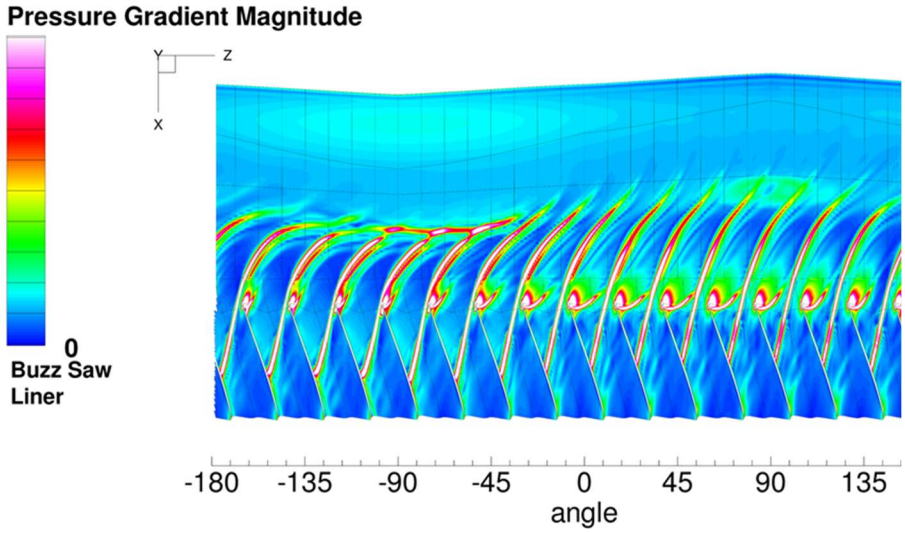

b) liner

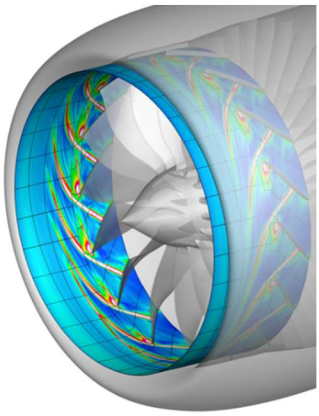

c) orientation

Fig 7 - Instantaneous pressure gradient contour levels at a near-wall cylinder, cross comparison of hard wall (a) and liner (b) in polar coordinates (streamwise coordinate versus azimuth angle). The orientation of the cylinder is visualized in (c), the keel is located at $-90°$ and the crown at $+90°$. The blades move counter-clockwise in (c) or in the negative angle direction (a) and (b). Red-pink-white contour levels mark shock structures. These contours were generated for the 'double-angle cosine' stacking.

C. Spectral Analysis of Buzz saw Noise and Blade Stacking

A Fourier transform of the computed pressure signal is obtained at an observer point located in the upper part of the highlight plane (y=0m, z=1m=0.88%R). The resulting spectra feature distinctively elevated sound pressure levels at the tones corresponding to the blade passing frequencies, engine orders #16, #32, and #48, **Fig 8a**. The blade passing frequency tones contribute to tonal noise in any operating condition. Buzz saw noise is characterized by excited tones at engine orders below the first blade passing frequency.

The hard wall spectrum of the 'double-angle cosine' stacking displays such elevated tones at engine orders ± 2 and ± 6 above and below the blade passing frequencies. The hard wall spectrum of the 'alternate' stacking features many of such excited tones. Most of its tones have roughly similar sound pressure level with minor alteration between odd (elevated) and even (depressed) tones. The 'alternate' stacking's tones at engine orders ± 1 and ± 2 above and below the blade passing frequencies are significantly weaker.

The configurations that are equipped with the liner model display notably reduced noise levels at moderate and high engine order tones, **Fig 8b**. The liner seems ineffective at attenuating noise levels at the lowest engine order tones. Optimal attenuation is observed near the liner's design frequency, engine order #42, and near engine order #10.

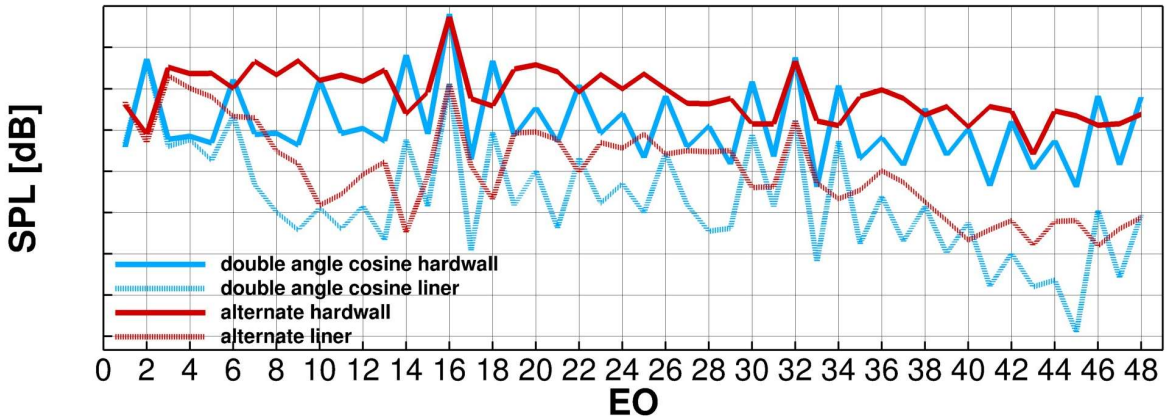

a) Sound pressure levels of both hard wall and liner configurations

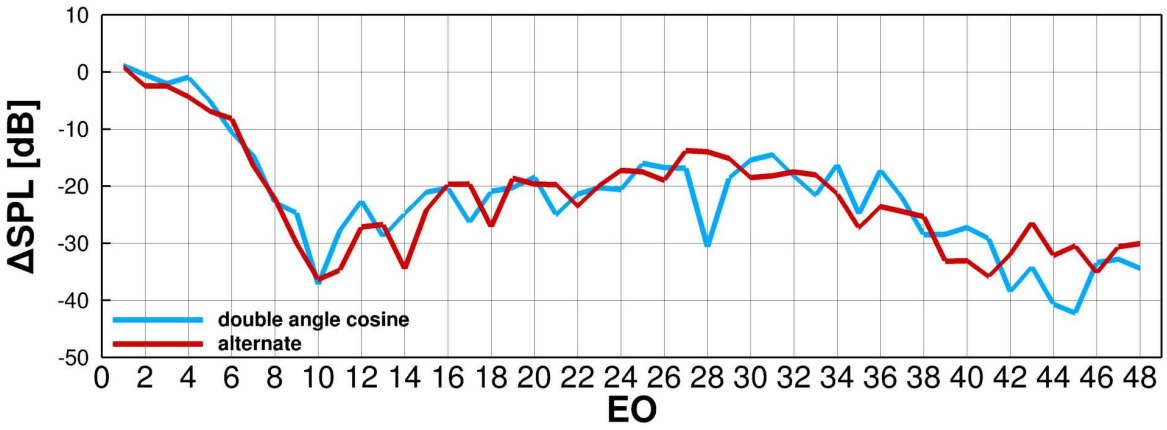

b) Level of attenuation

Fig 8 - Computed acoustic spectrum of observer that is located in the upper part of the highlight plane. The Engine Order (EO) is the frequency corresponding to the engine's rate of revolution. The first blade passing frequency tone corresponds to engine order #16.

The buzz saw noise spectrum is distinctly characterized by the applied stacking. The Fourier transform of the blade stacking orders are computed to investigate the relation between the applied stacking and the resulting noise spectrum, **Fig 9**. The 'double-angle cosine' stacking magnitude features exactly the same elevations at engine orders #2, #6, #10 and #14. The 'alternate' stacking magnitude's similarity to the associated acoustic spectrum is less pronounced. Its engine order #2, #6, #10 and #14 tones are weaker than the 'double-angle cosine' stacking in both the stacking magnitude and the obtained acoustic spectrum.

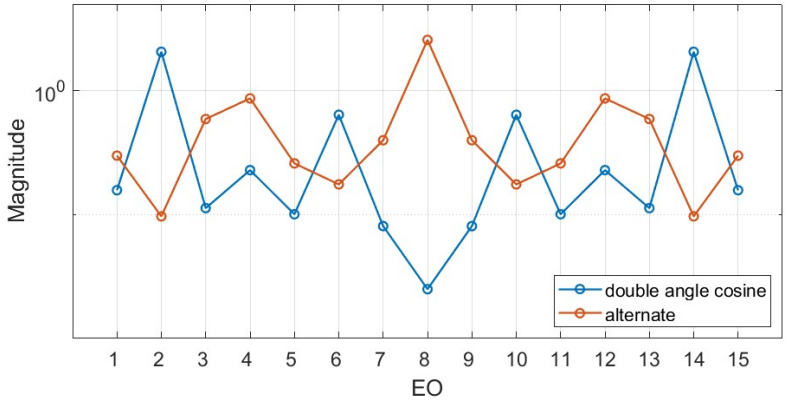

Fig 9 – Magnitude of Fourier transform of stacking order distributions of the applied blade twist deviation angles.

D. Near Field Acoustic Propagation

The Fourier decomposition of the pressure distribution is computed on the outer nacelle and highlight plane for distinct tones of the 'double-cosine stacking'. These tones are the low frequency buzz saw tones at engine orders #2, #6, #10 and #14, and the fundamental blade passing tones at engine orders #16, #32 and #48, **Fig 11**. The hard wall tones are not axisymmetric, **Fig 11a**. The asymmetry is the result of both the inflow angle-of-attack, and the supersonic region in the keel, which blocks outward propagating acoustic waves in that direction. The liner is effective at reducing the asymmetry, **Fig 11b**. The level of attenuation is in agreement with the results obtained at the observer point in the highlight, **Fig 8b**, i.e. a moderate reduction of noise levels is observed at engine orders #6, #16 and #32, a significant reduction at engine orders #10, #14 and #48, and a minor reduction at engine order #2.

A method based on the Ffowcs Williams – Hawkings integral equations is employed to investigate the acoustic directivity. The highlight plane, outer nacelle surfaces, and bypass and core duct exhaust planes form an enclosed surface that is used as the source mesh, **Fig 10a**. The interference pattern was computed at observer points on a sphere with radius of 10 m from the origin of the fan entrance, **Fig 10b**. The resulting sound pressure levels of the dominant 'double-angle cosine' tones are shown in **Fig 12**. The hard wall result displays significantly enhanced noise levels in the 10 o'clock region, **12a**. The liner is very effective at reducing this asymmetry significantly, improving noise levels in that direction, **12b**.

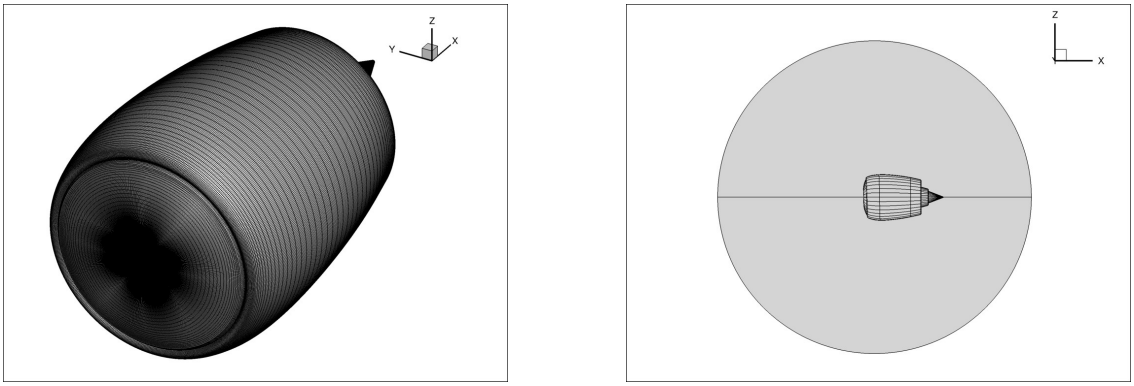

a) source mesh **b) observer mesh position**

Fig 10 – FW-H setup, the source mesh is composed of the outer nacelle and the highlight plane, the observer mesh is a sphere with radius of 10m with origin at the fan-face.

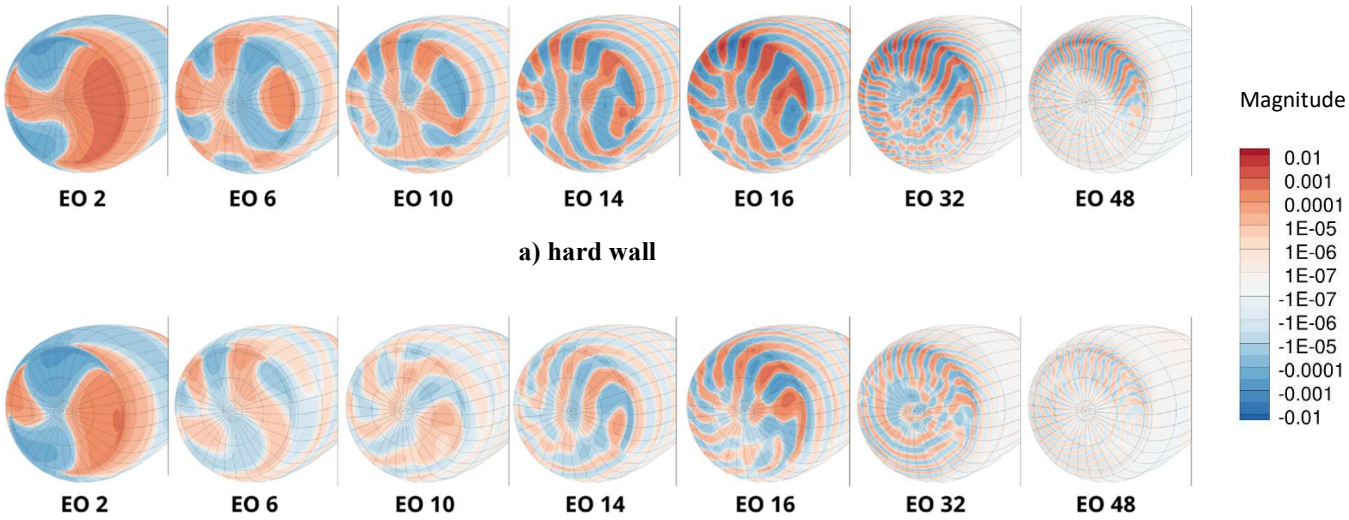

Fig 11 – Pressure Fourier modes (real part) at the outer nacelle and highlight plane of the distinct engine order tones of the 'double-angle cosine' stacking.

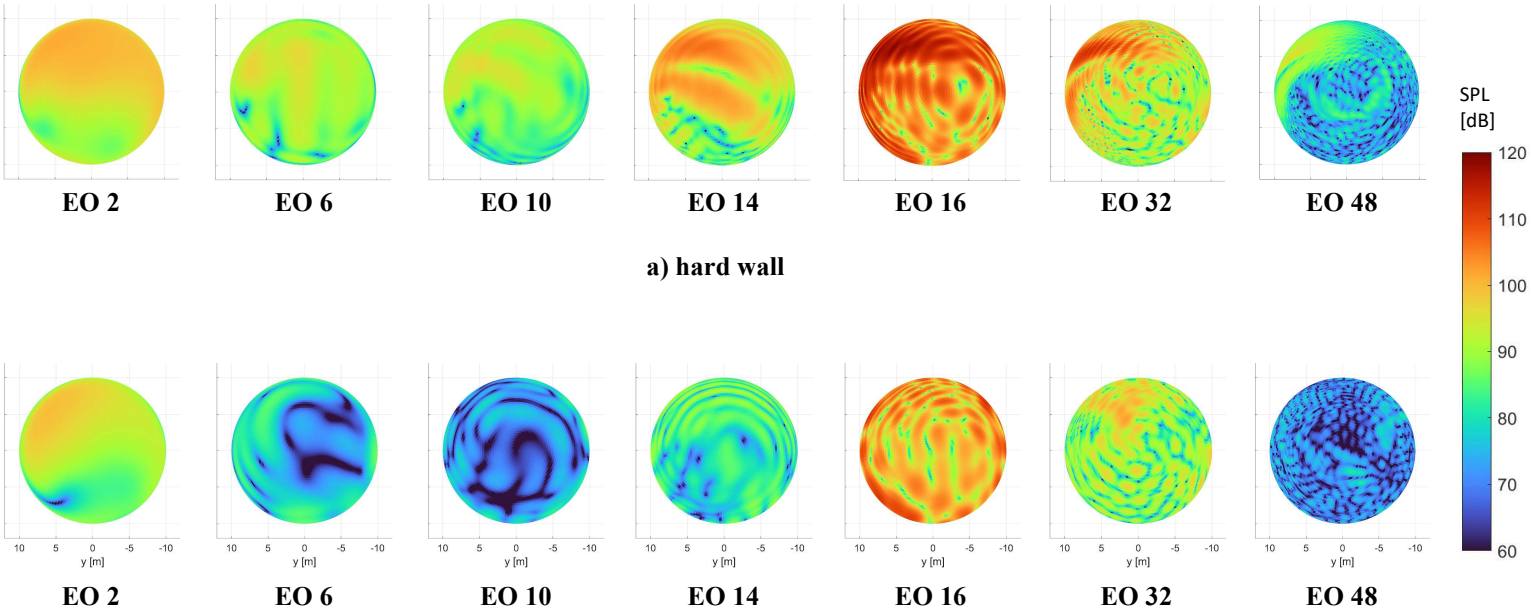

Fig 12 - Contour levels of the Sound Pressure Level (SPL) of the dominant 'double-cosine' stacking tones at a near-field sphere with radius of $10m$ from the fan entrance plane. The sphere is shown from an upstream perspective, as if the observer is looking into the fan. High SPL's are colored with red, moderate with yellow, and low blue.

E. Liner Dynamics

This section briefly illustrates the dynamics of the introduced liner impedance model. The liner model displays highly non-uniform characteristics, i.e. resistance and eigenfrequency, in the intake. The liner model acts as a porous wall, producing a non-zero wall-normal mass flux, **Fig 13a**. The non-linear resistance term, **Eq (4)**, contains a vortex shedding term (2nd term), which reacts to the amplitude of the liner flux, and a grazing flow term (3rd term). The isentropic Mach number at the wall is used to approximate the grazing flow Mach number, **Fig 13b**. Both terms contribute to the resulting non-linear resistance, **Fig 13c**. The resistance near the fan is dominated by the vortex shedding term, note the blade passing pattern near the fan, whereas the grazing term dominates near the highlight, note the gradient that matches the grazing Mach distribution near the highlight. The resonance frequency of the liner depends on the local wall temperature as well as higher-order terms, **Eq (9)**. The liner may get detuned at very high pressure levels near the fan, **Fig 13d**.

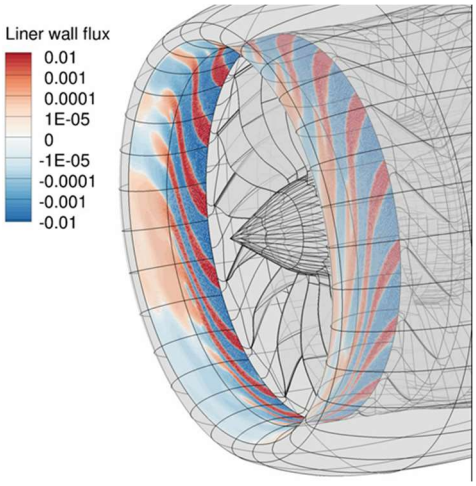

a) Liner wall-normal transpiration, red corresponds to suction (CFD outward), blue to injection (CFD inward).

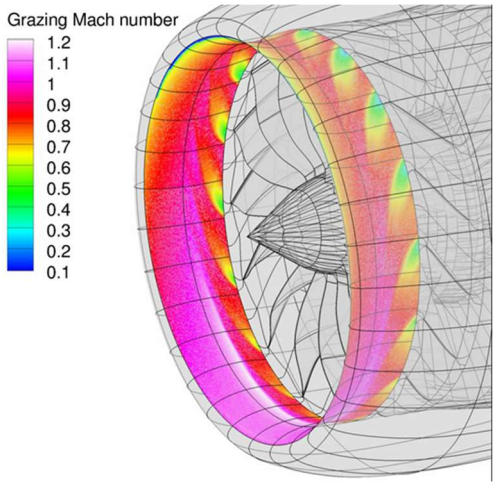

b) Isentropic Mach distribution that is used to compute the non-linear liner resistance term.

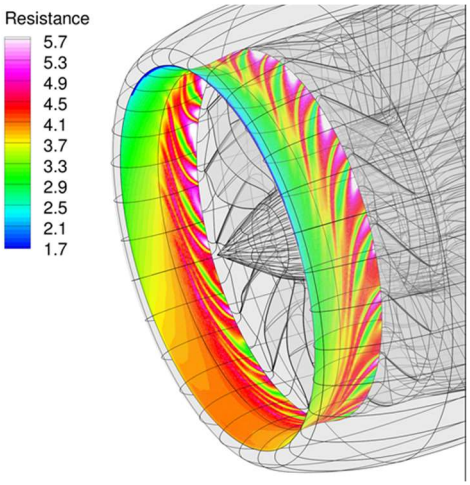

c) Computed non-linear resistance term

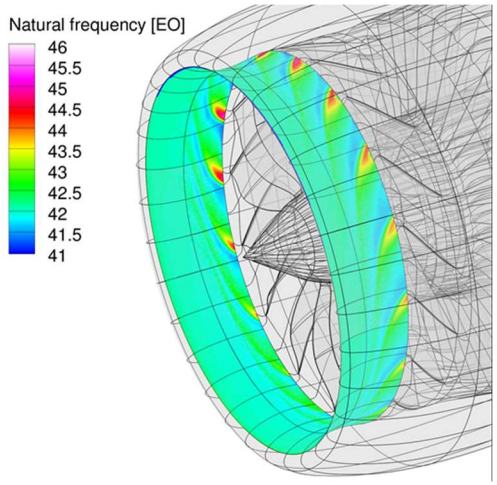

d) Natural frequency of the liner

Fig 13 – Instantaneous distributions that illustrate the mechanics of the liner impedance model.

IV. Discussion

Time-accurate simulations of the ASPIRE UHBR were realized to study its buzz saw noise characteristics. Blade loading perturbations were modeled by applying blade twist deviations. The order in which these twist deviations are arranged in azimuth affects the resulting buzz saw noise spectrum. Certain buzz saw tones may be enhanced or suppressed, which is shown in this work by considering two types of stacking orders. Additional simulations were performed to study liner attenuation. The lined cases show a significant reduction of overall noise levels, particularly in the direction of the 10 o'clock region. The liner is ineffective at attenuating low engine-order buzz saw tones. A realistic acoustic spectrum was obtained while including combined effects of the buzz saw noise generating mechanism and acoustic liners in a generic UHBR engine. The liner's characteristics are non-linear, depend on local grazing flow, sound pressure level, and wall-temperature. The most important next step would be to validate these results with experimentally obtained data.

Future research may improve time-accurate modeling of acoustic lining. The dynamics of the liner jets and grazing flow are likely not well captured in the current model. Furthermore, it is important to validate the time-accurate liner model far into the non-linear regime, i.e. sound pressure levels of at least 130dB, for which experimental results are scarce.

The liner model indicates that inlet lining features highly localized performance traits. Research of non-uniform liner designs could potentially better exploit local characteristics improving liner performance.

Finally, the results display liner-induced thrust variations up to 2%. A next step could be the inclusion of an aeroelastic model of the blades to study the relation of liners with blade mechanical vibrations.

Appendix : Description of the Liner Impedance Model

The considered liner wall treatment is a single-degree-of-freedom type honeycomb with perforated plate resistive sheet with given geometry cavity depth L, porosity σ, plate thickness t, and orifice diameter d. The geometric dimensions were determined by Habing and van der Meulen [8] for experimental scaling activities.

The time domain liner model was derived using momentum and mass balances, similar to the approach by Rienstra and Singh [9]. The resulting model is a non-linear low frequency approximation of the Helmholtz resonator. The model was complemented with modelling terms described by Guess [10].

The resulting model has the form of a driven harmonic oscillator,

$$\frac{\partial}{\partial t}\begin{bmatrix} q_w \\ p_0 \end{bmatrix} + \begin{bmatrix} \frac{r}{m} & \frac{1}{m} \\ -k & 0 \end{bmatrix}\begin{bmatrix} q_w \\ p_0 \end{bmatrix} = \begin{bmatrix} \frac{1}{m} \\ 0 \end{bmatrix} p_w \,, \tag{1}$$

with p_w the wall pressure, q_w the wall-normal mass-flux, p_0 the cavity pressure, the mass term m representing the inertial characteristics of oscillating air column,

$$m = \frac{1}{\sigma}\left(\frac{4}{3}t + \frac{1}{3}L\sigma + \Delta_G\right), \tag{2}$$

the spring term k representing the stored potential in the cavity,

$$k = \frac{1}{L}\left(a_w^2 + \frac{\gamma - 1}{2}M_n^2\right), \tag{3}$$

and the resistance term r representing damping.

$$r = \frac{C_r}{\sigma\rho_n} + \frac{1-\sigma^2}{\sigma}\left(\frac{|q_w|}{\rho_n\sigma} + kM_g a_w\right). \tag{4}$$

Note that positive q_w corresponds to flow into the liner, i.e. suction. In **Eq's (1)** to (**4**), Δ_G denotes Guess' orifice end-correction term,

$$\Delta_G = 0.85d\left(1 - 0.7\sqrt{\sigma}\right)\frac{1 + 5\cdot 10^3 M_n^2}{1 + 10^4 M_n^2}\frac{1}{1 + 305M_g^3}, \tag{5}$$

in which M_n denotes the Mach number in the orifice neck,

$$M_n = \frac{1}{\sigma}\frac{q_w}{\rho_w a_w}, \tag{6}$$

M_g the grazing Mach number, which is approximated in the intake by taking the local isentropic Mach number, C_r is the Poiseuille resistance term with Guess' correction,

$$C_r = \frac{32\mu(t+d)}{d^2}, \tag{7}$$

and ρ_n the density in the orifice neck, which is approximated in an upwind manner,

$$\rho_n = \rho_0(1 - \operatorname{sgn} q_w) + \rho_w(1 + \operatorname{sgn} q_w)\,, \tag{8}$$

with $\rho_0 = p_0/RT_w$. Furthermore note that a is the speed of sound, p the pressure, ρ the mass-density, T temperature, R specific gas constant, μ the dynamic viscosity. Subscript w denotes a variable at the wall, subscript n a variable at

the orifice neck, and subscript *0* a variable in the cavity. Finally, constant k is fixed at 0.3. The undamped natural frequency ω_0 of the model is given by

$$\omega_0 = \sqrt{\frac{k}{m}}. \tag{9}$$

Acknowledgements

NLR carried out this study in the framework of the PROPMAT project cooperating with Airbus. NLR has received funding from the European Union's H2020 program for the Clean Sky Joint Technology Initiative under grant agreement number 680954.

Disclaimer

The document reflects only the author's view; the JU is not responsible for any use made of the information contained herein.

References

[1] A. McAlpine, M. Fisher and B. Tester, "Buzz-saw' noise: A comparison of modal measurements with an improved prediction method," *Journal of Sound and Vibration,* vol. 306, pp. 419-443, 2007.

[2] M. Laban, J. Kok and a. H. Brouwer, "CFD/CAA analysis of UHBR engine tonal noise," in *AIAA/CEAS Aeroacoustics Conference*, Atlanta, 2018.

[3] M. Méheut, F. Sartor, M. Vergez, M. Laban, R. Schnell, A. Stuermer and G. Lefevre, "Assessment of fan/airframe aerodynamic performance using 360° uRANS computations: Code-to-code comparison between ONERA, DLR, NLR, and Airbus," in *AIAA Scitech 2019 Forum*, San Diego, 2019.

[4] M. Daroukh, C. Polacsek and A. Chelius, "Shockwave generation and radiation from an UHBR engine with flow distortion using a CFD/CAA chaining strategy," in *25th AIAA/CEAS aeroacoustics conference*, Delft, 2019.

[5] F. Menter, "Two-equation Eddy-viscosity turbulence models for engineering applications," *AIAA Journal,* vol. 32, pp. 1598-1605, 1994.

[6] J. Kok, "A high-order low-dispersion symmetry-preserving finite-volume method for compressible flow on curvilinear grids," *Journal of Computational Physics,* vol. 228, 2009.

[7] C. Tam and J. Webb, "Dispersion-relation-preserving finite difference schemes for computational acoustics," *Journal of Computational Physics,* vol. 228, pp. 262-281, 1993.

[8] R. Habing and M. v. d. Meulen, "Design considerations of acoustic liners for scaed test models," in *Aviation forum 2021*, Virtual event, 2021.

[9] D. Singh and S. Rienstra, "A systematic impedance model for non-linear helmholtz resonator liner," in *19th AIAA/CEAS Aeroacoustics Conference*, Berlin, 2013.

[10] A. Guess, "Calculation of perforated plate liner parameters from specified acoustic resistance and reactance," *Journal of Sound and Vibration,* vol. 40, no. 1, 1975.